Revealing deformation mechanisms in additively manufactured Alloy 718: Cryogenic to elevated temperatures

Nabeel Ahmad [a,b], Reza Ghiaasiaan [a,b], Paul R. Gradl [c], Shuai Shao [a,b], Nima Shamsaei [a,b,*]

[a] National Center for Additive Manufacturing Excellence (NCAME), Auburn University, Auburn, AL, 36849, USA
[b] Department of Mechanical Engineering, Auburn University, Auburn, AL, 36849, USA
[c] NASA Marshall Space Flight Center, Propulsion Department, Huntsville, AL, 35812, USA

A B S T R A C T

Tensile behavior of Alloy 718, fabricated through laser powder directed energy deposition, was examined over a wide temperature range (−195, 25, 200, 425, 650, 870, and 980 °C). The tensile properties, deformation mechanisms, and their temperature dependence were specifically investigated. The microstructure and mechanical properties were characterized in fully heat treated condition; i.e., first stress relieved, then homogenized, then solution annealed, and finally 2-step-aged. Tensile results showed thermally stable behavior from room temperature up to 650 °C, similar to other additively manufactured and wrought counterparts. Rapid reductions of strength with increasing test temperature were observed at −195 to 25 °C and 650–870 °C ranges, which were respectively ascribed to a significant reduction in deformation twinning density and the coarsening of γ''-precipitates as confirmed by electron microscopy. The fully heat treated microstructure also contained populous Mo/Nb-rich carbides within grain interior which were observed to be the dominant mechanism of fracture and responsible for the temperature insensitive ductility up to 650 °C. At 870 and 980 °C, sliding between dynamically recrystallized grains became significant resulting in an increased ductility.

1. Introduction

Alloy 718 [1] is a γ'-γ''-precipitation hardened Ni-base superalloy and is known for excellent strength, creep, and fatigue resistance [2–4]. It is therefore particularly attractive for use in extreme service applications such as cryo-tanks, housings, manifolds, nuclear reactors, and gas turbines – many of them also require components to be in complex shapes [5]. However, Alloy 718 has poor machinability because of its high strength and hardness [6]. As a result, conventional manufacturing of Alloy 718 parts with machining has been challenging and costly. Recently, additive manufacturing (AM) has received increasing attention from various industries because of its capability to fabricate complex geometries on demand economically, thereby significantly improving design freedom, reducing the need for machining and assembly operations, and reducing material waste [7,8]. Such advantages over conventional manufacturing combined with Alloy 718's decent fabrication characteristics such as weldability due to its low Ti and Al content have made Alloy 718 a popular material for various AM processes [9,10].

Due to the typical thermal characteristics of AM processes such as high cooling rates [11], the non-heat treated (NHT) microstructure of Alloy 718 is often dendritic and lacks strengthening precipitates, leading to compromised strength compared to the fully heat treated (HT) condition [12–16]. In addition, the thermal history associated with different AM technologies, including electron beam powder bed fusion (E-PBF) [13], laser beam powder bed fusion (L-PBF) [15], laser powder directed energy deposition (LP-DED) [17], and laser wire directed energy deposition (LW-DED) [14], can be significantly different due to inherently different process characteristics, such as power of energy sources, travel speed of the molten pool, inter-layer time, and substrate temperature [18], to name a few.

The unique thermal history of each process greatly affects the microstructure and mechanical properties of Alloy 718 in the NHT condition. For example, Deng et al. [10] reported that the NHT Alloy 718 fabricated via E-PBF possessed higher hardness and strength, but similar ductility compared to NHT L-PBF. This was attributed to the presence of strengthening precipitates in E-PBF produced specimens. Specimens fabricated using the same technology, but varied process parameters, could also result in significantly different microstructures (including grain size and degree of micro-segregation) and mechanical properties. For instance, Zhu et al. [17] revealed that decreasing the

Abbreviations and nomenclature

AGE	Double aging
Alloy 718	Nickel base (Inconel 718) superalloy
AM	Additive manufacturing/additively manufactured
BSE	Backscattered electron
DRX	Dynamic recrystallization
E-PBF	Electron beam powder bed fusion
EBSD	Electron backscatter diffraction
EDS	Energy dispersive x-ray spectroscopy
EL	Elongation to failure
GB	Grain boundary/boundaries
HOM	Homogenization
HT	Heat treatment/heat treatments/heat treated
IPF	Inverse pole figure
K	Strength coefficient
KAM	Kernel average misorientation
L-PBF	Laser beam powder bed fusion
Longitudinal plane	Plane parallel to build direction
LP-DED	Laser powder directed energy deposition
LW-DED	Laser wire directed energy deposition
$M_{23}C_6$	Cr-rich metal carbide
M_6C	Mo-rich metal carbide
MC	Metal carbide
NHT	Non-heat treated
n	Strain hardening exponent
Radial plane	Plane perpendicular to build direction
SA	Solution annealing
SEM	Scanning electron microscope/scanning electron microscopy
SR	Stress relief
STEM/FIB	Scanning transmission electron microscope/Focused ion beam
UTS	Ultimate tensile strength
YS	Yield strength
γ -grain	Ni-matrix
γ''- phase	Gamma double prime (Tetragonal Ni_3Nb with DO_{24} structure)
ε_p	True plastic strain
σ_{true}	True stress

laser power (higher cooling rate) of LP-DED Alloy 718 resulted in finer dendrites and the formation of discrete Laves, while increasing the laser power (lower cooling rate) returned coarser dendrites. Tensile results showed similar ductility, but yield strength (YS) and ultimate tensile strength (UTS) of specimens with finer dendrites were 17% and 9% higher, respectively, than those of the coarser dendritic ones.

The microstructural differences in Alloy 718 resulting from variations in the processing conditions may even persist after standardized heat treatment (HT) schedules are applied, which could result in different mechanical responses. For example, Schneider [19] exhibited that Alloy 718 fabricated using LW-DED, LP-DED, and L-PBF, with HT procedures according to AMS 5664 and AMS 5663 [20,21], resulted in large differences in grain size, degree of homogenization, and tensile properties. Microstructural characterizations and mechanical testing results revealed that the L-PBF grain structure was more refined and homogenized and had two times the ductility of LW-DED and LP-DED processes. Similarly, studies by Blackwell et al. [22] on LP-DED, Trosch et al. [15] on L-PBF, and Deng et al. [23] on E-PBF Alloy 718 showed that the standard AMS 5662 HT cycle on the Alloy 718 specimens fabricated by these technologies would result in different tensile properties. Results indicated that YS of LP-DED Alloy 718 specimens was 7% and 15% higher compared to L-PBF and E-PBF specimens, while their ductility was 35% lower than L-PBF and 43% lower than E-PBF specimens. Such differences in tensile properties are also expected at elevated temperatures. For example, YS and ductility of L-PBF Alloy 718 [15] specimens tested at 650 °C were, respectively, 5% and 67% higher than those of the E-PBF specimens [13].

Despite Alloy 718 being extensively studied, knowledge on its behavior from cryogenic to elevated temperature is quite scattered even for its wrought form [24], a comprehensive study in this regard therefore is lacking. For the AM forms of this alloy, most studies in the literature report its tensile properties at room temperature [25]. The knowledge on the temperature dependence of these properties remains scarce, although limited data exist for the L-PBF form [15]. Notably, the cryogenic mechanical properties of AM Alloy 718 are specifically lacking from the literature.

Therefore, there is a need for a careful evaluation of the microstructure and mechanical properties of Alloy 718 fabricated via different routes. Such considerations should be made over the wide application temperature range of this alloy such as the ones experienced by aerospace components [5]. The objective of this work was to study the uniaxial tensile behavior of fully HT LP-DED Alloy 718 at different temperatures of −195, 25, 200, 425, 650, 870, and 980 °C. Its microstructural evolution during multiple stages of HT based on AMS 5664 [21] was first examined and analyzed. Thorough microstructural and fractographic analyses were also performed to correlate mechanical properties with the deformation and fracture mechanisms. This article is arranged as the following: in Section 2, the experimental procedure is described. In Section 3, experimental results, including initial microstructures (Section 3.1), tensile properties (Section 3.2), and deformed microstructures (Section 3.3) are presented. The findings of this study are discussed in detail in Section 4, emphasizing on the effect of test temperature on YS (Section 4.1), and fracture mechanism (Section 4.2). Finally, conclusions are drawn in Section 5.

2. Materials and methods

Pre-alloyed Alloy 718 powder (diameter range: 45–150 μm) supplied by AP&C [26] consisted of predominantly spherical particles and was produced using plasma rotating electrode process. The chemical composition of the Alloy 718 powder, listed in Table 1, was in accordance with specifications set by ASTM B637 [27] and AMS 5596 [28]. The original cylindrical bars, later to be machined into test specimens,

Table 1
Chemical composition of Alloy 718 powder (according to AP&C certificate) used for this study.

LP-DED Alloy 718	
Element	Composition (wt.%)
Ni	Bal.
Cr	19
Fe	16
Nb	5.3
Mo	3
Co	1
Ti	0.9
Al	0.6
Si	0.4
Mn	0.35
Cu	0.3
C	0.08
S	0.02
P	0.015
B	0.006
O	0.008

were deposited vertically by the RPM Innovations, Inc. using a 222 LP-DED machine. The process parameters used for deposition were as the following: laser power of 1070 W, powder feed rate of 0.26 g/s, scanning speed of 16.9 mm/s, and layer thickness of 0.381 mm.

2.1. Heat treatment procedure

The cylindrical bars were removed from the build plate using a band saw and then HT in a vacuum furnace. Temperature histories were recorded using various thermocouples embedded with the specimens. HT cycle included stress relief (SR), homogenization (HOM), solution annealing (SA), and double aging (AGE) (see Table 2). The microstructural evolution during multiple HT stages was tracked using small witness coupons, which were excised from cylindrical bars. The HT cycle is based on ASTM and AMS specifications which have the heritage to wrought Alloy 718 [29,30].

2.2. Test specimens and mechanical testing

Cylindrical bars were machined to the final dimensions according to ASTM E8 [32] standard (see Fig. 1). The uniaxial tensile tests were performed at seven different temperatures ranging from cryogenic (at −195 °C), room (at 25 °C), and elevated temperatures (at 200, 425, 650, 870, to 980 °C). The mechanical testing at room temperatures was performed based on the ASTM E8 [32] standard. The cryogenic and elevated temperature tensile tests were conducted according to the ASTM E21 standard [33]. Prior to the actual mechanical testing at the cryogenic temperature, the test specimens were pre-soaked in liquid N_2 for 5 min, to achieve steady-state thermal condition. For elevated temperature tests, the test specimens were pre-heated at the corresponding elevated temperatures for 30 min. The tensile tests were conducted at the nominal strain rate of ~0.005 mm/mm/min under displacement-controlled loading condition until failure. An extensometer was attached to the specimens only for the initial 0.050 mm/mm strain for accurate calculation of the YS and the modulus of elasticity. Afterwards, it was removed due to the device's limited travel. Note that each tensile property reported in this study is the mean value obtained

using at least six repetitive tests.

2.3. Metallography and microscopy

The microstructures on the radial plane, i.e., perpendicular to the build direction, of the small witness coupons (10 mm diameter by 5 mm height) extracted at different HT stages was examined using a Zeiss Crossbeam 550 scanning electron microscope (SEM). Postmortem microstructures on the longitudinal plane, i.e., parallel to the build direction, were also examined from small coupons excised from the test specimens using an abrasive cutter. Metallography procedures were carried out according to the ASTM-E3 standard [34]. The coupons were mounted using epoxy molding then ground using various silicon carbide papers ranging from 220, 320, 400, 600, and 1000 grits applied with light contact pressure and followed by a final polishing procedure using 0.05 μm colloidal silica with water.

The Zeiss SEM was equipped with a focused ion beam (FIB) column, a scanning transmission electron microscopy (STEM) detector, and Oxford onboard instruments such as the energy dispersive x-ray spectroscopy (EDS) and electron backscatter diffraction (EBSD) detectors. Grain size measurements were obtained from EBSD analysis (excluding the annealing twins) using the Aztec Crystal software from Oxford Instruments. The criterion used to detect grain boundaries (GBs) from the inverse pole figure (IPF) maps was when the misorientation angle between two adjacent pixels was >10°. Backscattered electron (BSE) micrographs were obtained by the electron channeling contrast imaging technique [35] using the four-quadrant backscattered electron detector. STEM lamella was prepared by a Ga^+ FIB milling procedure at 30 kV with excessively reducing current from 7 nA to 100 pA followed by lift-out. FIB polishing on the lamella was performed at 30 kV with a reducing current from 100 pA to 10 pA, resulting in a final thickness of <70 nm.

The fracture surfaces were further sonicated in isopropanol solution for better removal of contaminants. The SEM micrographs of fracture surfaces were obtained using 15 kV voltage, 1 nA current, and 9 mm working distance. The EBSD and EDS analyses were performed with 70° and 54° pre-tilt holders, respectively, at 8–10 mm working distance, 20 kV voltage, and 3 nA current. The EBSD and EDS maps were obtained using a step size of ~3 μm and an exposure time of 3 ms, respectively. STEM micrographs were taken within the Zeiss Crossbeam with the STEM detector under the imaging conditions of 30 kV voltage and 110 pA current.

3. Results

3.1. Initial microstructure

The NHT microstructure, as shown by the IPF maps in Fig. 2(a) on the radial plane, was a mixture of fine and coarse grains. Moreover, the orientation of a high fraction of grains of red color suggested a strong texture along <001>. Such structures are typical of NHT LP-DED Alloy 718 with grain growth in the build direction [36,37]. Coarsening of a limited degree was caused by the SR treatment, although the <001>

Table 2
HT cycle applied to the specimens with the designation of each step [29,30].

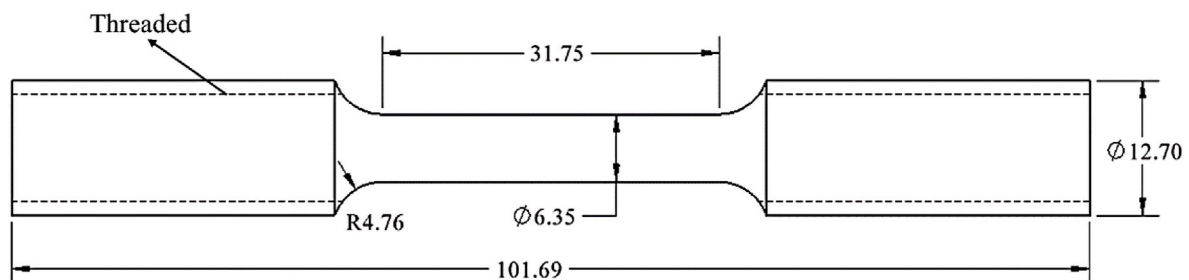| Procedure	Temperature	Time	Quench	Reference
(Designation)	(°C)	(hr)		
Stress Relief (SR)	1065	1.5	2 bar Argon gas at 20 °C/min	ASTM F3055 [30]
Homogenization (HOM)	1162	3.5		[31]
Solution Annealing (SA)	1065	1		AMS 5664 [21]
Double Aging (AGE)	760	10	Furnace cool at 10 °C/min	AMS 5664 [21]
	650	10	3 bar Argon gas at 20 °C/min	

Fig. 1. Drawing of the tensile specimen based on ASTM E8 [32] standard (all dimensions are in mm).
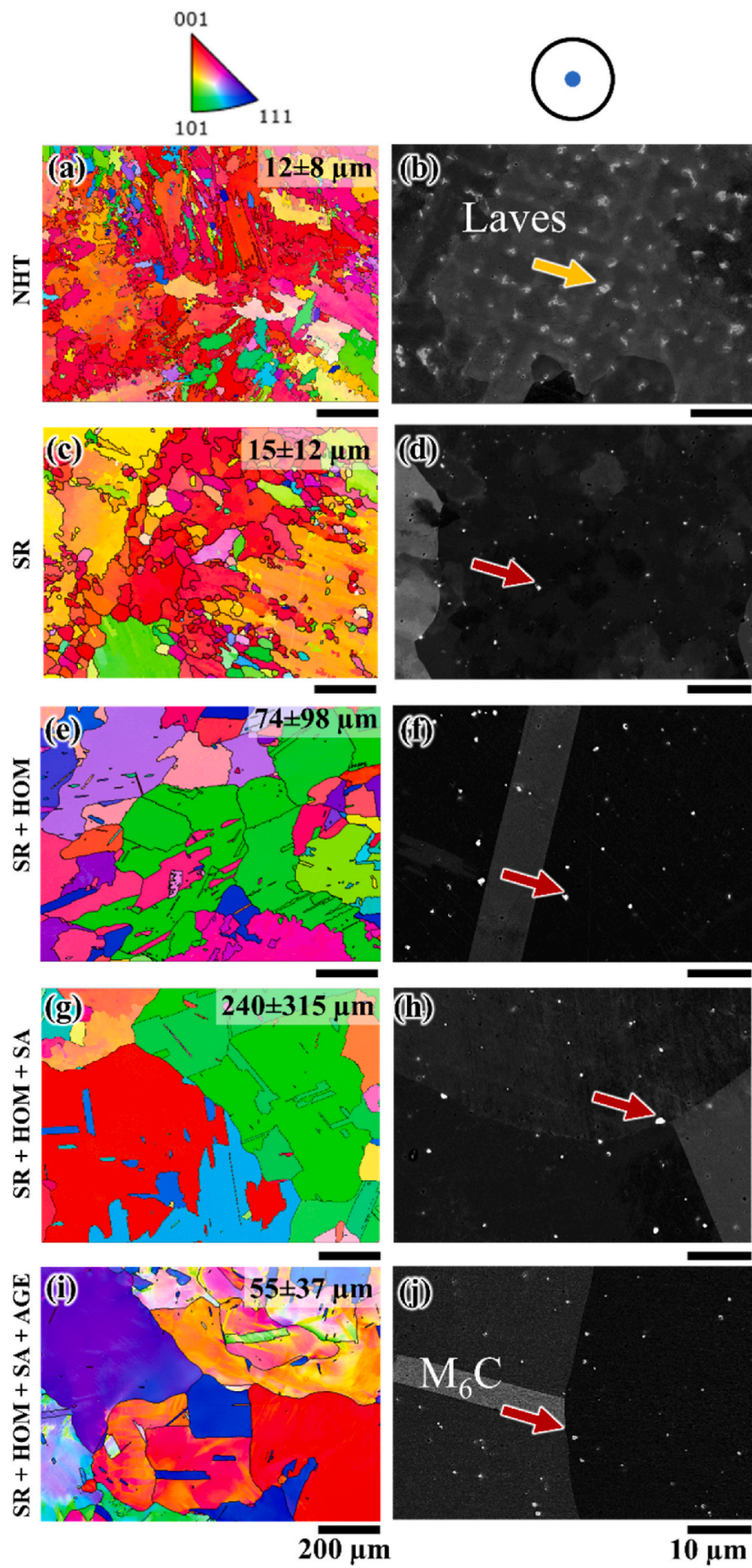
Fig. 2. IPF maps and BSE micrographs of LP-DED Alloy 718 in various stages of HT: (a)–(b) NHT, (c)–(d) SR, (e)–(f) SR + HOM, (g)–(h) SR + HOM + SA, and (i)–(j) SR + HOM + SA + AGE.
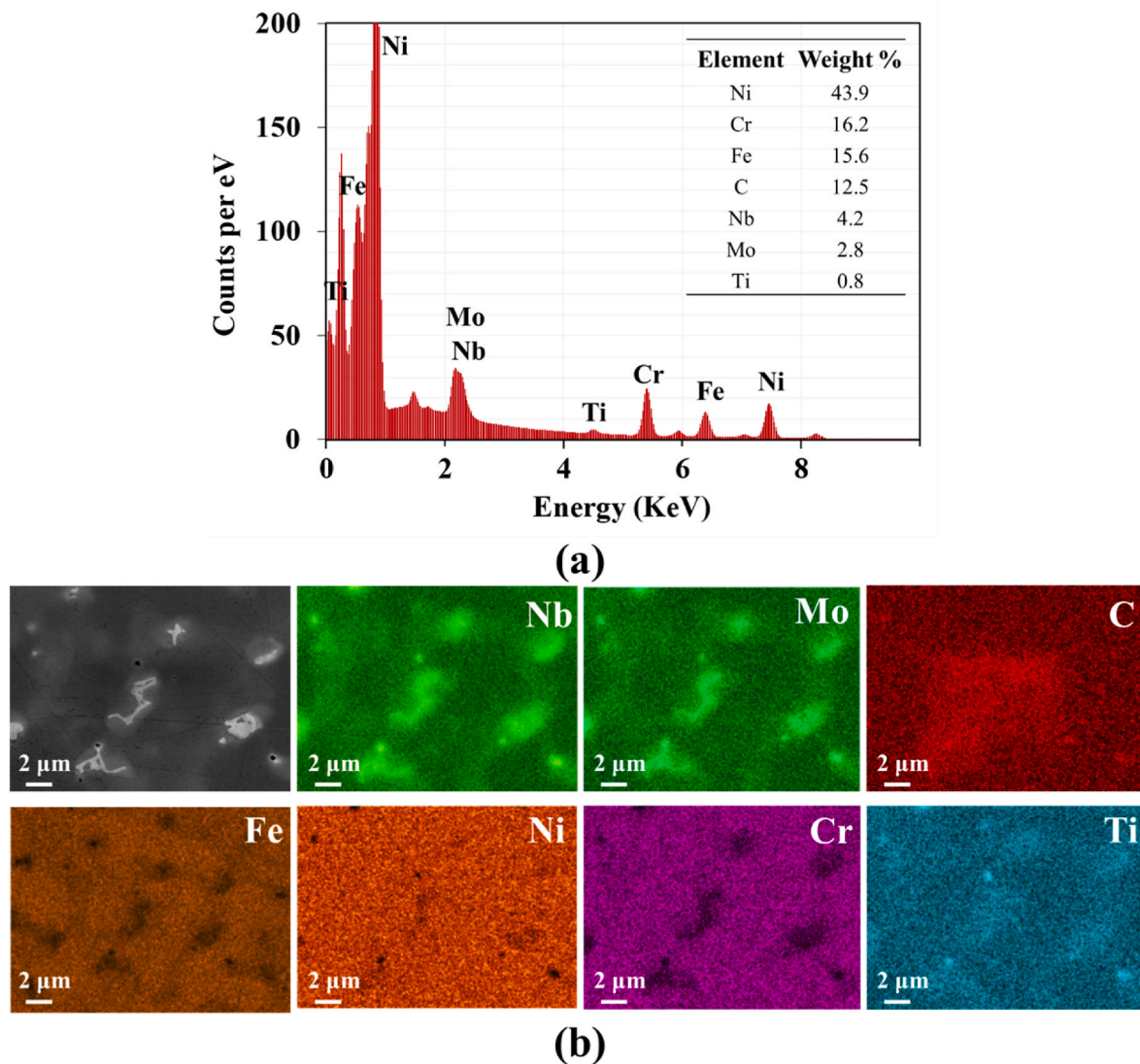
Fig. 3. Results from EDS, including (a) X-ray spectrum, and (b) elemental maps, performed on an NHT LP-DED Alloy 718 sample showing enriched/depleted elements existing in inter-dendritic regions.

texture was not significantly affected (as shown in Fig. 2(c)). Following HOM significant grain growth occurred, and excessively large grains (diameter >500 μm) and annealing twins dominated the microstructure (see Fig. 2(e)). Although grain growth continued during SA at 1065 °C for 1 h (see Fig. 2(g)), it was not as significant compared to the growth during the HOM step, which had a longer isothermal holding time (3.5 h) at a relatively high temperature (1162 °C). These observations were echoed by the work of Qi et al. and Mostafa et al. [38,39]. In comparison, the largest grains in the L-PBF counterpart in the same HT condition were well below 100 μm [40]. Furthermore, following HOM and SA steps, the microstructures appeared to have lost their strictly <001> texture as grains with more random orientations nucleated and grew. After the AGE step, the γ″ phase was formed [41], which will be shown and discussed in Section 4.1.

BSE micrographs (see Fig. 2(b)) showed that the NHT microstructure of LP-DED Alloy 718 was dendritic and had precipitates of irregular shapes in the inter-dendritic regions. Following SR at 1065 °C, the dendritic microstructure partially broke down. This implied that the temperature and/or relatively short duration (~1.5 h) of SR was not sufficient to completely dissolve microscale elemental segregation and the partially stabilized dislocation cells [17,38]. Following HOM at a significantly higher temperature of 1162 °C, the dendritic structure was

completely removed (see Fig. 2(f)). This can be attributed to the relatively high temperature of HOM and prolonged soaking duration compared to SR, which lead to a better homogenization effect.

The inter-dendritic regions in the NHT condition, as indicated by EDS (see Fig. 3) were rich in Nb, Ti, and Mo, while depleted in Fe and Cr. Although C was also seen to slightly concentrate, the C-rich regions did not collocate with the Nb-, Ti-, and Mo- rich ones. This Nb- and Ti-rich phase could thus be Laves phase, consistent with the available reports in the literature [15,37,42–46]. Laves is a brittle and hard phase and is generally considered harmful for mechanical properties [50,51]. Such microstructure in NHT specimens could be ascribed to high solidification rates of AM processes [25,47,48]. Several studies have demonstrated that Laves phase tends to dissolve above 1060 °C, which is the range of the SR stage of this study [31,49]. As expected, Laves phase diminished post-SR and the segregation pattern is replaced by several bright particles in the intergranular and transgranular locations as indicated by arrows in Fig. 2(d), (f), (h) & (j). In addition, HOM and SA stages appeared to have grown the carbides slightly.

Elemental maps of these carbide particles (see Fig. 4) obtained from the fully HT condition revealed the concentration of Nb, Mo, Ti, and C, which suggested that they could be carbides of type MC, M_6C, or $M_{23}C_6$ [46], all of which are FCC compounds. EBSD scans recognized these
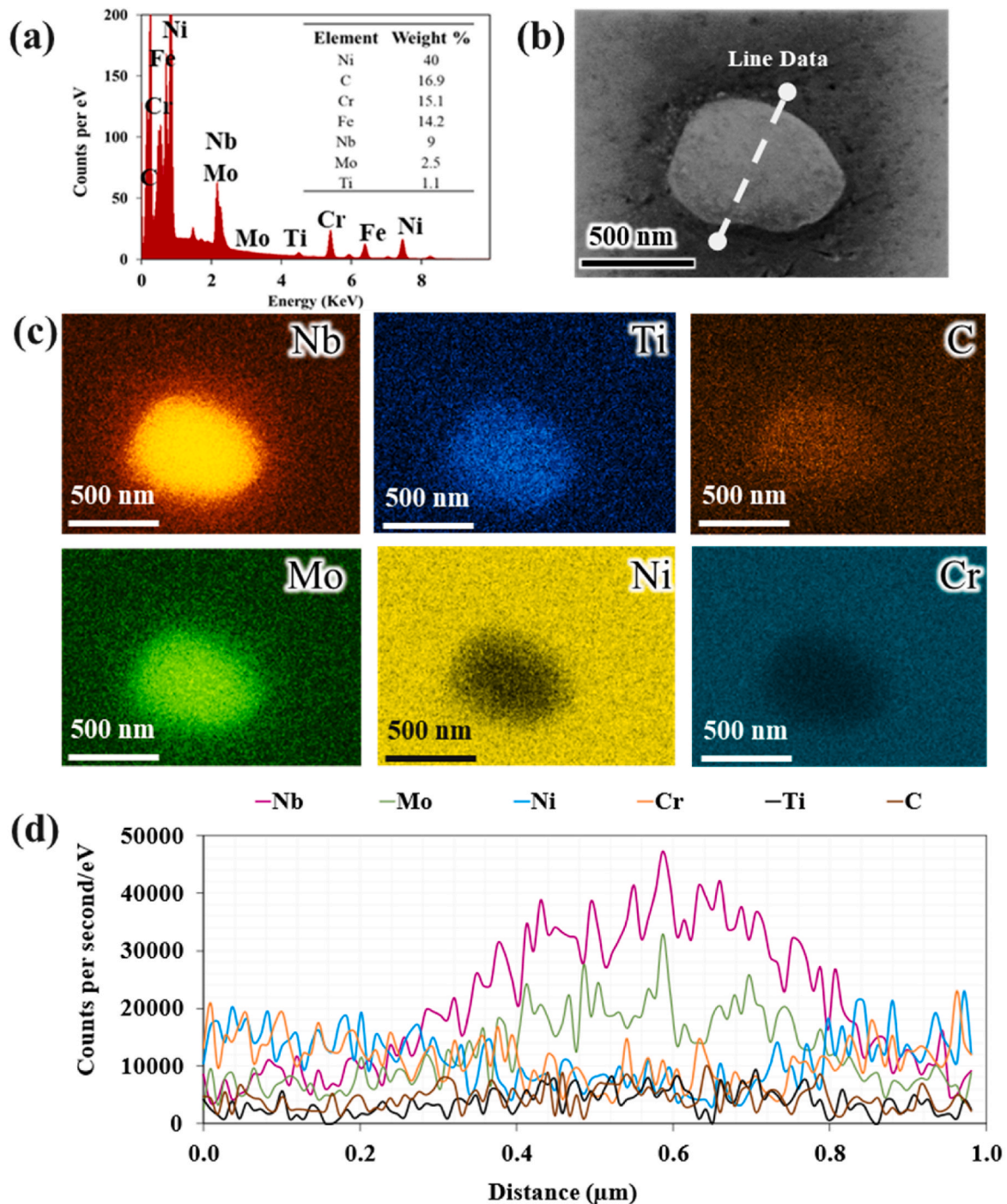
Fig. 4. Results from EDS, including (a) X-ray spectrum, (b) BSE image of the bright particle along with the line profile (c) elemental maps, and (d) line profiles, performed near the bright particles of the fully HT LP-DED Alloy 718 sample.

carbides as an FCC phase (see discussion in Section 4.2). Line profiles revealed the count of C element to be significantly lower than the metallic elements, which further confirmed the identity of these carbides to be either M_6C or $M_{23}C_6$ [25–28]. Note that M_6C are Mo-rich carbides and typically form at intermediate temperatures (e.g., 1038 °C), while $M_{23}C_6$ are Cr-rich carbides and precipitate at low temperatures (i.e., 790-816 °C) [46], which suggested that these carbides could be M_6C.

3.2. Tensile properties

Representative true stress – true strain curves for each test temperature is shown in Fig. 5(a). The stress response was observed to be highest at −195 °C, followed by a gradual decrease with an increase in test temperature between 25 and 650 °C. At 870 and 980 °C, the stress response dropped drastically which hints at a change in deformation mechanism. Furthermore, uniaxial tensile properties of the LP-DED Alloy 718; i.e., YS, UTS, and elongation to failure (EL) examined in this study at different temperatures are presented in Fig. 5(b). As shown, the mechanical properties of the LP-DED alloy were relatively stable
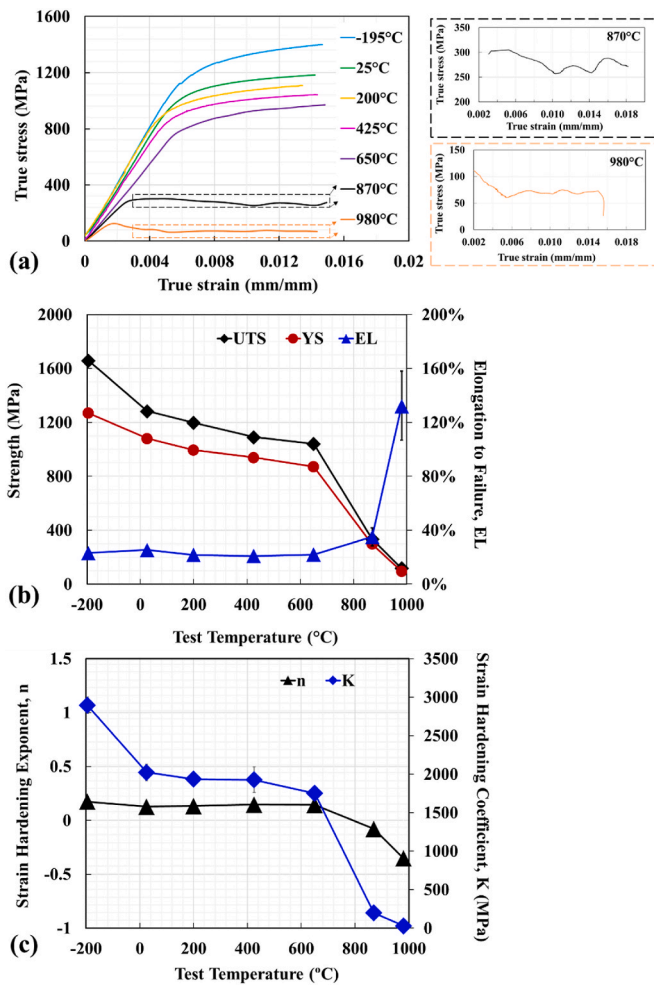
Fig. 5. Tensile properties of LP-DED Alloy 718 in fully HT condition at different test temperatures of −195, 25, 200, 425, 650, 870, and 980 °C: (a) true stress – true strain curves (one curve from each test temperature is shown), (b) average UTS, YS, and EL, and (c) average of *n* and K. Standard deviation at each test temperature is also shown in (b) and (c).

between room temperature and 650 °C, exhibiting only a slight reduction of strengths (~20% reduction in YS, and UTS) and almost no change in ductility with increasing temperature. Interestingly, at −195 °C the alloy had similar ductility and much higher strength as compared to the room temperature properties. At temperatures above 650 °C, an abrupt change in tensile response; i.e., a significant reduction in strength and increase in ductility, occurred which is consistent with the reported data for the wrought counterpart in the literature (see Fig. 6).

In concomitant with the sudden drop in the tensile strength at temperatures above 650 °C, the post-yield behavior transitioned from strain hardening to strain softening. This is further shown in Fig. 5(c) where the average strain hardening exponent (*n*) turned negative above 650 °C. The exponents were obtained by fitting the post-yield portions of the true stress-true strain curves (up to a strain of ~0.015 mm/mm) with a power law; i.e., $\sigma_{\text{true}} = K (\varepsilon_p^n)$, where K is the strength coefficient, ε_p is the true plastic strain, and σ_{true} is the true stress [52]. The strength coefficient data is also reported in Fig. 5(c). The strength coefficient versus test temperature followed a similar trend as yield strength; rapid changes between −195 and 25 °C, as well as above 650 °C. The error bars in Fig. 5(b) and (c) are the standard deviation among 6 data points collected for each test temperature. Except at 980 °C, the error bars at most of the temperatures were not visible in the figures because of low scatter in the data obtained from repeated tests.

As a benchmark, the tensile properties of the LP-DED Alloy 718

obtained from this study are compared with those of its counterparts reported in the literature [13,15,24] and presented in Fig. 6. As shown, the overall negative correlation of strength and test temperature observed in this study was similar to that seen for other manufacturing processes; i.e., E-PBF (reported by Sun et al. [13]), L-PBF (reported by Trosch et al. [15]), cast (reported by Trosch et al. [15]), and wrought (reported by Ono et al. [24], Trosch et al. [15], and Haynes International [2]). At the cryogenic temperature of −195 °C, the tensile strength of the LP-DED Alloy 718 (this study) was similar to wrought [24] as shown in Fig. 6(a) and (b).

At test temperatures of 25, 200, and 425 °C, the strength obtained in this study under the LP-DED condition was slightly lower than the ones reported for wrought and L-PBF conditions. Moreover, EL measured in this work for LP-DED Alloy 718 was slightly higher compared to the ones for L-PBF and wrought counterparts reported by Trosch et al. [15] (see Fig. 6(c)). This could be attributed to the relatively large population of needle-shaped δ precipitates in the L-PBF and wrought specimens reported by Trosch et al. [15]. The closely spaced δ phase particles are known to provide abundant sites for void nucleation under quasi-static tensile loading and result in reduced EL. In contrast, the volumetric density of carbide particles observed in this work was significantly lower than that of δ precipitates reported by Trosch et al. [15], which led to higher EL seen in this study.
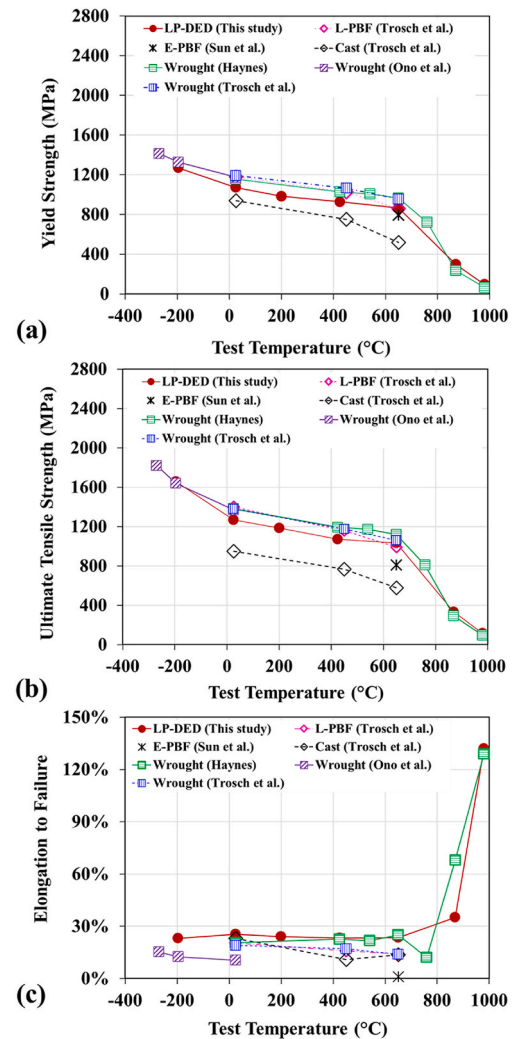

Fig. 6. Tensile properties of LP-DED Alloy 718 at different test temperatures obtained in this study compared to the data reported in the literature: (a) YS, (b) UTS, and (c) EL. Literature data include those of the wrought [2,15,24], L-PBF [15], E-PBF [13], and cast [15] counterparts.

3.3. Deformed microstructure

The IPF along with the kernel average misorientation (KAM) maps for all the specimens fractured at different temperatures obtained from the longitudinal cross section (i.e., the plane parallel to the build direction) close to fracture surface are presented in Fig. 7. The KAM maps estimate the local misorientation within grains, lattice distortion, as well as plastic strains which are indicators of geometry necessary dislocation
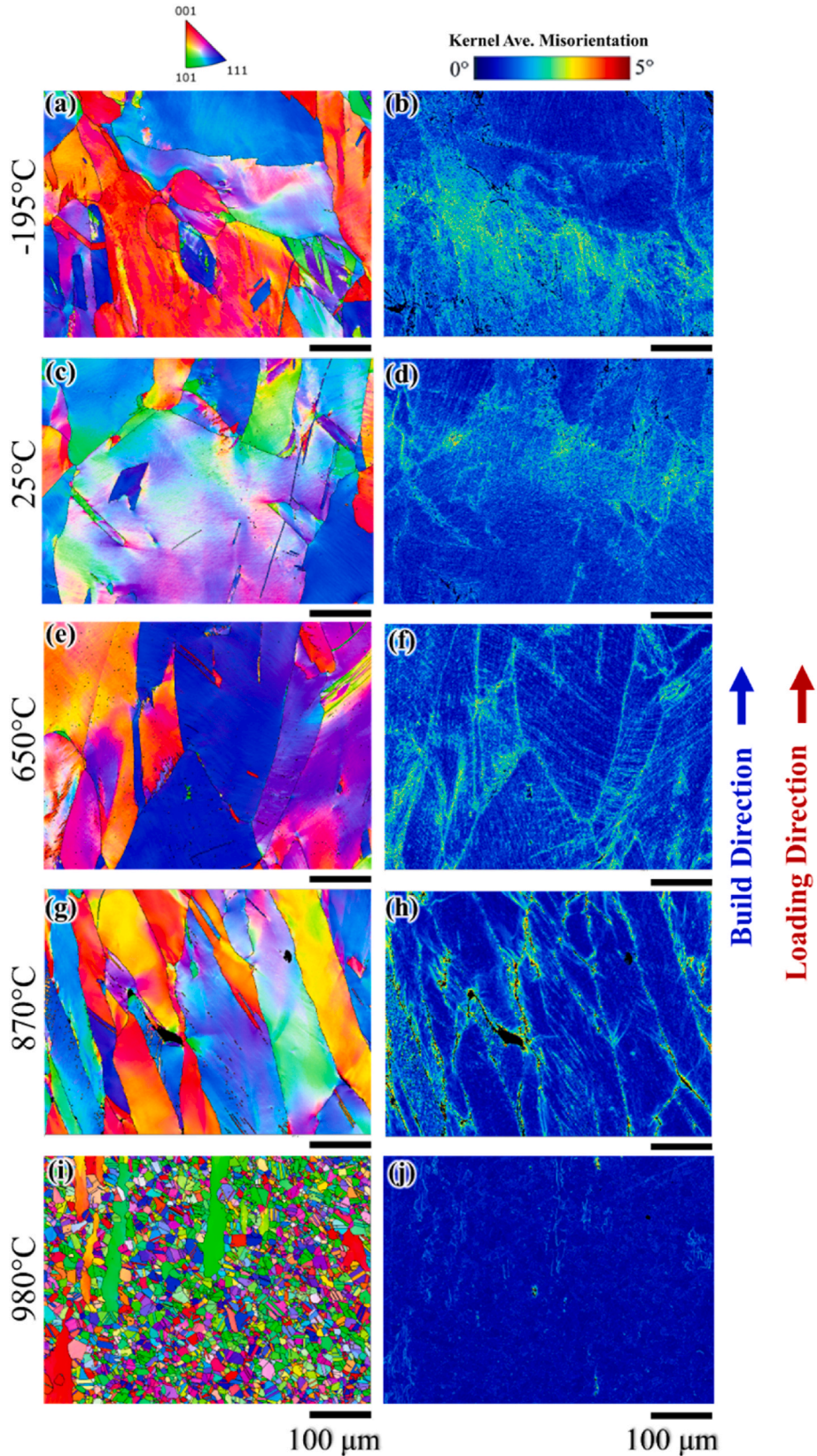

Fig. 7. IPF and KAM maps of the HT LP-DED Alloy 718 examined on the longitudinal cross sections of specimens fractured at: (a)–(b) −195 °C, (c)–(d) 25 °C, (e)–(f) 650 °C, (g)–(h) 870 °C, and (i)–(j) 980 °C.

density and twinning activities [44]. A kernel size of 3 by 3 steps with a step size of ~500 nm was used for KAM analysis. Moreover, the color scale of KAM maps was set from 0 to 5°, and the misorientation angles due to GBs were excluded. From Fig. 7, the local misorientations appeared more severe between test temperatures of −195 and 650 °C than at 870 and 980 °C, indicating a higher amount of transgranular plastic deformation.

The reduced misorientations at 870 and 980 °C (Fig. 7(h) & (j)) were likely due to significant dynamic recrystallization (DRX). Other high temperature recovery processes such as dynamic recovery (i.e., via the annihilation of dislocations, cross-slip, and dislocation climb) are not as active because Alloy 718 has low stacking fault energy, and thus, DRX typically prevails in this temperature range [53]. This phenomenon tends to occur first at GBs. Early plastic deformation due to elastic mismatch between two grains can happen at GBs which then causes faster dislocation density rise which facilitates the nucleation of new grains [53,54]. The onset temperature of DRX observed in this study could be at 870 °C (~0.65 of melting temperature), which was consistent with the reported temperature of 850 °C for Alloy 718 [55]. The flow stress oscillations, observed for 870 and 980 °C (see Fig. 5(a)), could also be the result of the observed DRX. The undeformed microstructure contained GB carbides which were effective resistors of GB sliding. However, the recrystallized small grains at the prior GB regions were more likely to slide and accommodate plasticity and suppress the dislocation/twinning activity in the grain interior.

The size of DRX grains appeared to be strongly dependent on deformation temperature; the average DRX grain size grew with the increase in the test temperature, ~0.5 μm and ~14 μm at 870 °C and 980 °C, respectively. Moreover, the fraction of DRX grains also increased with the increase in deformation temperature, reaching DRX fraction from <1% at 870 °C to over 85% at 980 °C. This was attributed mainly to the enhanced diffusion rates leading to an increased growth activity of DRX grains [53]. The substantially grown DRX grains under 980 °C led to essentially zero misorientation field as shown in Fig. 7(j).

4. Discussions

4.1. Effect of test temperature on yield strength

The trend of decreasing YS of Alloy 718 with respect to temperature, shown in Fig. 6, is well documented in the literature (wrought [2,15,24], L- PBF [15], E-PBF [13], and cast [15] forms). The slightly lower strength reported from the present study compared to the literature could be due to the significantly coarser microstructure produced by the LP-DED process. As shown in Fig. 5(b), rapid change in the strength occurred at two temperature ranges; i.e., from −195 to 25 °C and from 650 to 980 °C. A similar "knee" in the strength – temperature relation at 650 °C was observed for wrought Alloy 718 [2], which was attributed to the coarsening of γ″ precipitates. However, such coarsening was typically reported after an isothermal holding time of at least 16 h [46,56] – the cause of the significant reduction in strength above 650 °C (such as at 870 °C) after a holding time of only 30 min needs further explanation. In addition, although already reported for the wrought Alloy 718 [24], the authors were not able to find an explanation in the literature for the alloy's significantly higher strength at the cryogenic temperature than other test temperatures.

In order to provide an understanding in this regard, thin lamellae were FIB milled and lifted out from the fractured tensile specimens near the fracture surfaces (~200 μm) and examined under the STEM mode in the SEM (see Fig. 8 for the bright field images). At −195 °C, Fig. 8(a) and (b) respectively reveal stripe patterns (the direction is indicated by the dashed line) and relatively small, tortuous γ″ precipitates in the deformed microstructure. The stripes appeared to be nanoscale deformation twins whose thickness was only a few nm with faint boundaries as they were not being viewed edge-on. Deformation twinning is favorable under cryogenic conditions since, unlike dislocation gliding

which requires the thermal nucleation/propagation of kinks and becomes difficult at lower temperatures, it is a displacive process that is relatively insensitive to temperature. This speculation is consistent with the tortuous morphology of the precipitates as they may have been sheared by the twins.

Although deformation twinning was also observed at room temperature, the twin density was much lower, and the twins were much thicker (up to 100 nm thick), as shown in Fig. 8(c) and (d). The precipitates outside of twins were in the well-known lens shape with little to no distortion, indicating little particle shearing by dislocations, which corroborates the argument made in the previous paragraph regarding precipitates being sheared by twins instead of dislocations. The high density of nanoscale twins formed during the cryogenic deformation process provided an additional barrier to the gliding of dislocations and could have contributed to the added strength compared to the room temperature and above. The contrast in the density of deformation twins was also reflected in the change in the intragranular misorientations, as shown in KAM (see Fig. 7(b) & (d)).

The test temperature up to 650 °C did not alter the morphology or size of the γ″ precipitates (compare Fig. 8(d) and (f)) which explains the somewhat plateau in strength observed between room temperature and 650 °C (see Fig. 5(b)). The very gradual decline of strength could partially be ascribed to the increasing mobility of dislocations with the increasing temperature. The easier dislocation glide made deformation twinning less favorable. Indeed, although deformation twinning was still present at 650 °C (Fig. 8(e)), it was much less prevalent compared to the specimen tested at the room temperature (Fig. 8(c)). The reduced density of deformation twins was likely another cause of the slight reduction in YS in this temperature range.

The pre-test holding at the higher temperature of 870 °C for 30 min had significantly coarsened the γ″ precipitates (diameter ~100 nm) and reduced their number density. These larger particles were much farther apart and thus expected to be incoherent with the γ matrix which was likely the primary reason for the pronounced reduction in strength at this temperature. In addition, although the deformation twins were absent in the STEM images of 870 °C specimen (Fig. 8(g)), they were apparently visible from the IPF maps taken on the longitudinal cross sections (see further discussion in Section 4.2). The deformation twins not being captured in the STEM images was likely due to the small window of observations (only a few μm). The coarsening of precipitates is expected to be much more severe under the higher temperature of 980 °C which lowered the strength even further.

4.2. Effect of test temperature on fracture mechanism and ductility

The EL of the alloy was not significantly affected by temperature until 650 °C, above which a noticeable increase occurred. The relatively stable EL in these temperatures indicated the same mechanism governing the fracture. Indeed, as shown in Fig. 9(c), (f) & (i), fracture surfaces for tests at/below 650 °C featured fine dimples of sub-micron size (~2 μm), suggesting a relatively ductile behaving fracture governed by the nucleation, growth, and coalescence of voids. Furthermore, angled views (see Fig. 9(a), (d) & (g)) for test temperatures below and equal to 650 °C revealed similar fracture morphology. In addition, fracture surfaces exhibited well-defined central regions surrounded by the shear lips, making an angle of 45° to the plane of fracture.

The vast majority of dimples observed at temperatures below 650 °C had fractured particles visible. These particles were characterized using EDS and results showed that most dimples contained several particles rich in Nb, Mo, Ti, and C (see the elemental maps in Fig. 10) – similar chemistry to that of the fine metal carbides dispersed throughout the grain interior (see Fig. 4). This suggested that the fracture mechanisms observed for test temperatures at/below 650 °C were due to the nucleation of voids that formed on the carbide/matrix interface debonding or fracture of carbides. During the onset of plastic deformation, carbides present in the γ-matrix obstruct the motion of dislocations. The pile-up
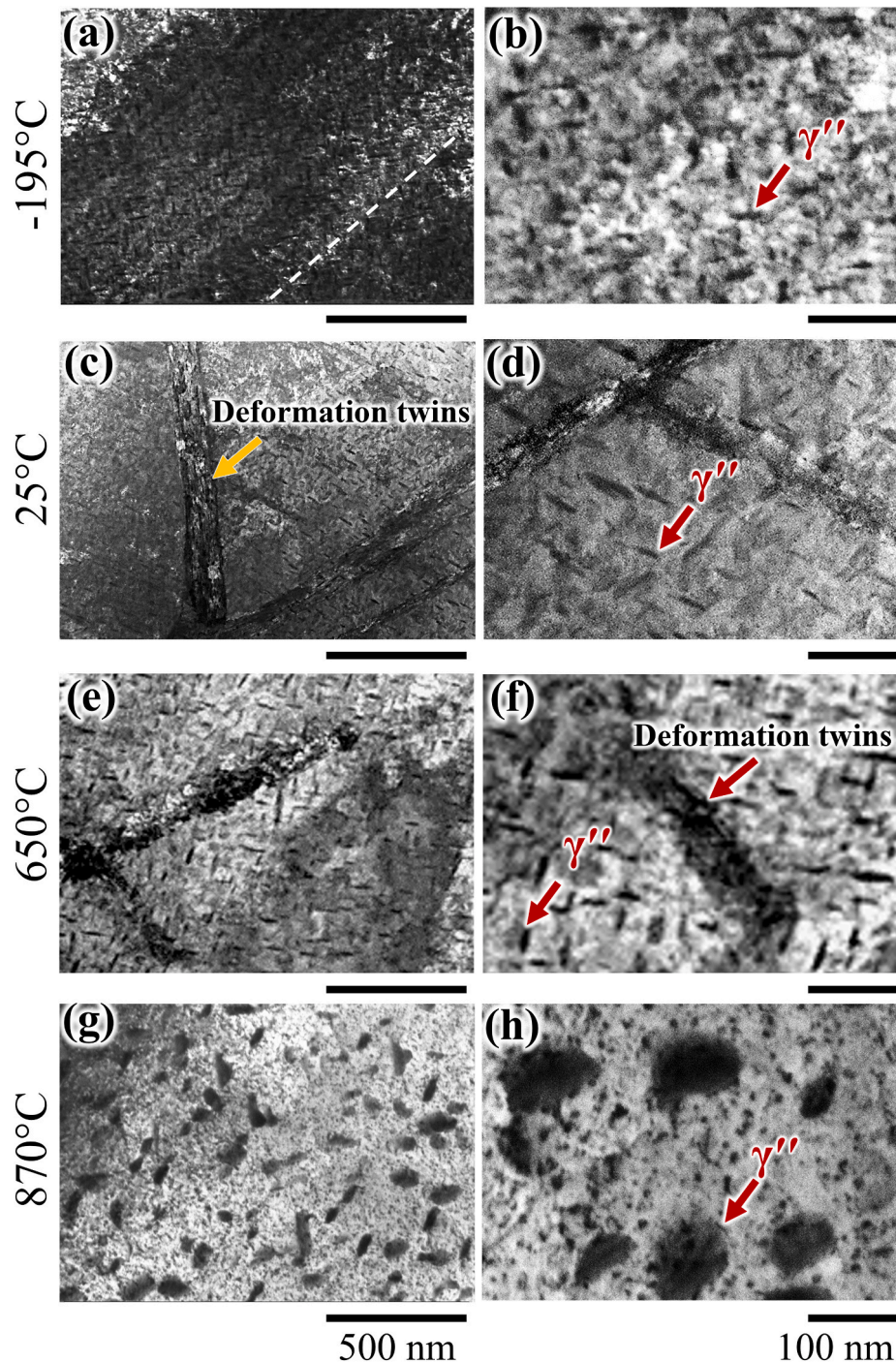
Fig. 8. Bright field STEM images revealing the details of γ″ precipitates and deformation twins in specimens tested at different temperatures: (a)–(b) −195 °C, (c)–(d) 25 °C, (e)–(f) 650 °C, and (g)–(h) 870 °C. Dashed white line in (a) indicates direction of deformation twins.

of these dislocations causes stress concentration around carbides. Once this stress reaches the bonding strength of carbide and γ-matrix, voids can form. BSE micrographs taken on the longitudinal cross sections of the fractured specimens showed vast majority of microscopic voids were nucleating from the metal carbides (see Fig. 11). Even the voids that did not appear pairing with carbides were still likely nucleated from them, as the plane of the cross section did not necessarily go through both a void and a carbide simultaneously. The proximity of microvoids facilitated the coalescence of microcracks that led to the fracture of the specimens.

At the higher test temperature of 870 °C, the noticeable increase in

EL indicated the onset of a new fracture mechanism. As shown in Fig. 9 (j)–(l), regions with well-defined fine dimples subsided in the fracture surfaces of 870 °C and were replaced by regions that show evidence of grain boundary cleavage. To understand the deformation behavior, EBSD analysis was performed on the longitudinal cross section and the results are presented in Fig. 12(a)-(d). It appears at 870 °C that DRX grains at the prior boundaries of the fully HT grains were nucleated, as seen in Fig. 12(b). Several deformation "bands", with a thickness of a few hundred nanometers, were also formed, as noticeable in Fig. 12(c). Fig. 12(d) shows the profile of misorientation angles across one of such bands, revealing 60° angles at the boundaries, confirming that these
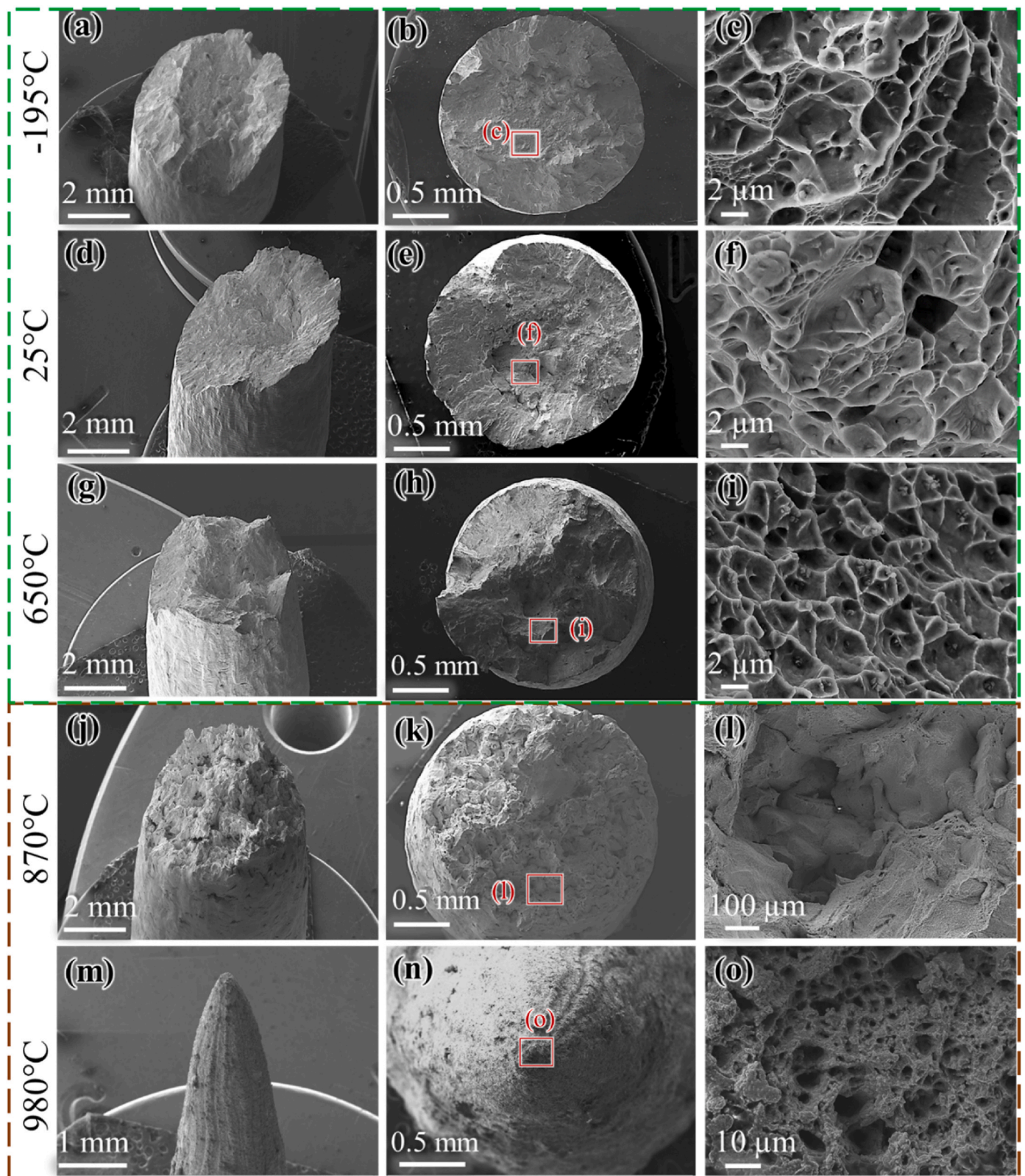
Fig. 9. Tensile fracture surfaces of LP-DED Alloy 718 specimens tested at different temperatures: (a)–(c) −195 °C, (d)–(f) 25 °C, (g)–(i) 650 °C, (j)–(l) 870 °C, and (m)–(o) 980 °C.
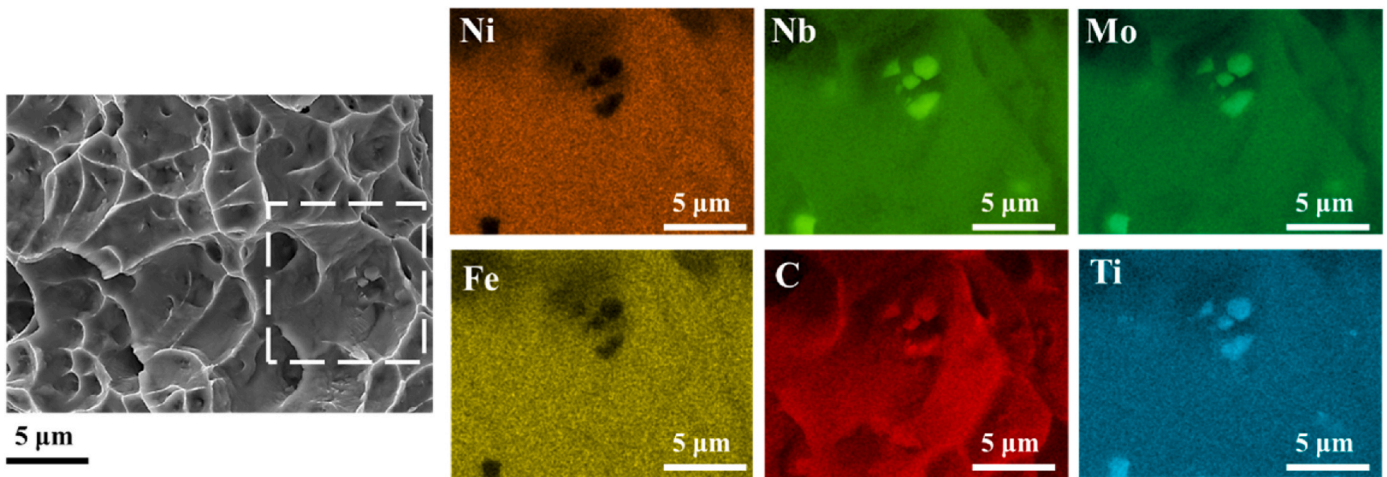
Fig. 10. EDS analysis of the tensile fracture surface of LP-DED Alloy 718 specimen tested at 200 °C, showing the carbides within the fine dimples.
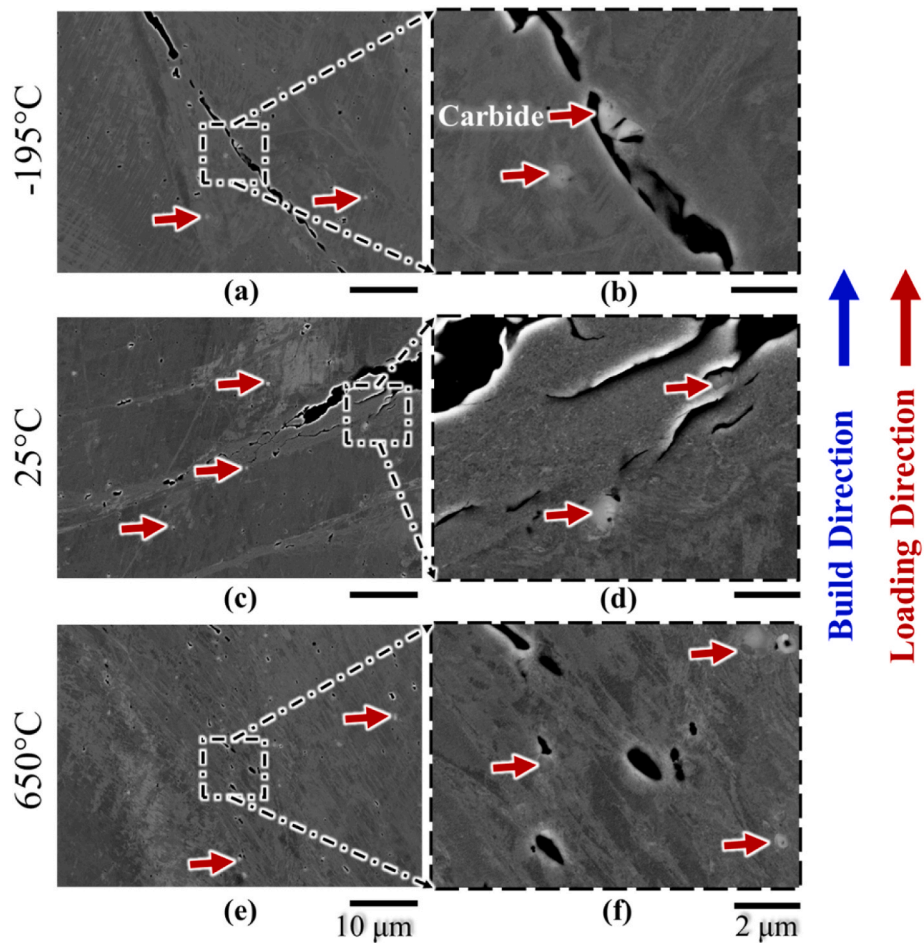

Fig. 11. BSE images of fractured specimens examined from the longitudinal plane at different test temperatures: (a)–(b) −195 °C, (c)–(d) 25 °C, and (e)–(f) 650 °C. Red arrows indicate carbides. (For interpretation of the references to color in this figure legend, the reader is referred to the Web version of this article.)

bands were indeed deformation twins. Small FCC particles, which were in fact carbide particles as confirmed by the EDS analysis mentioned earlier, were also detected in the EBSD image of the specimen tested at 870 °C (see Fig. 12(c)). DRX grains were susceptible to GB sliding, which coexisted with dislocation gliding and twinning as the plastic deformation mechanisms at 870 °C. In fact, the GB sliding was expected to be responsible for the improved ductility and the reduced strength at this temperature. In addition, the GB sliding replaced carbide fracturing/debonding and became the governing mechanism for nucleation of tensile cracks (see Fig. 12(a)–(c)).

At 980 °C, the fracture surfaces were completely conical, with the tip of the cones decorated with large voids, suggesting profuse ductility (see
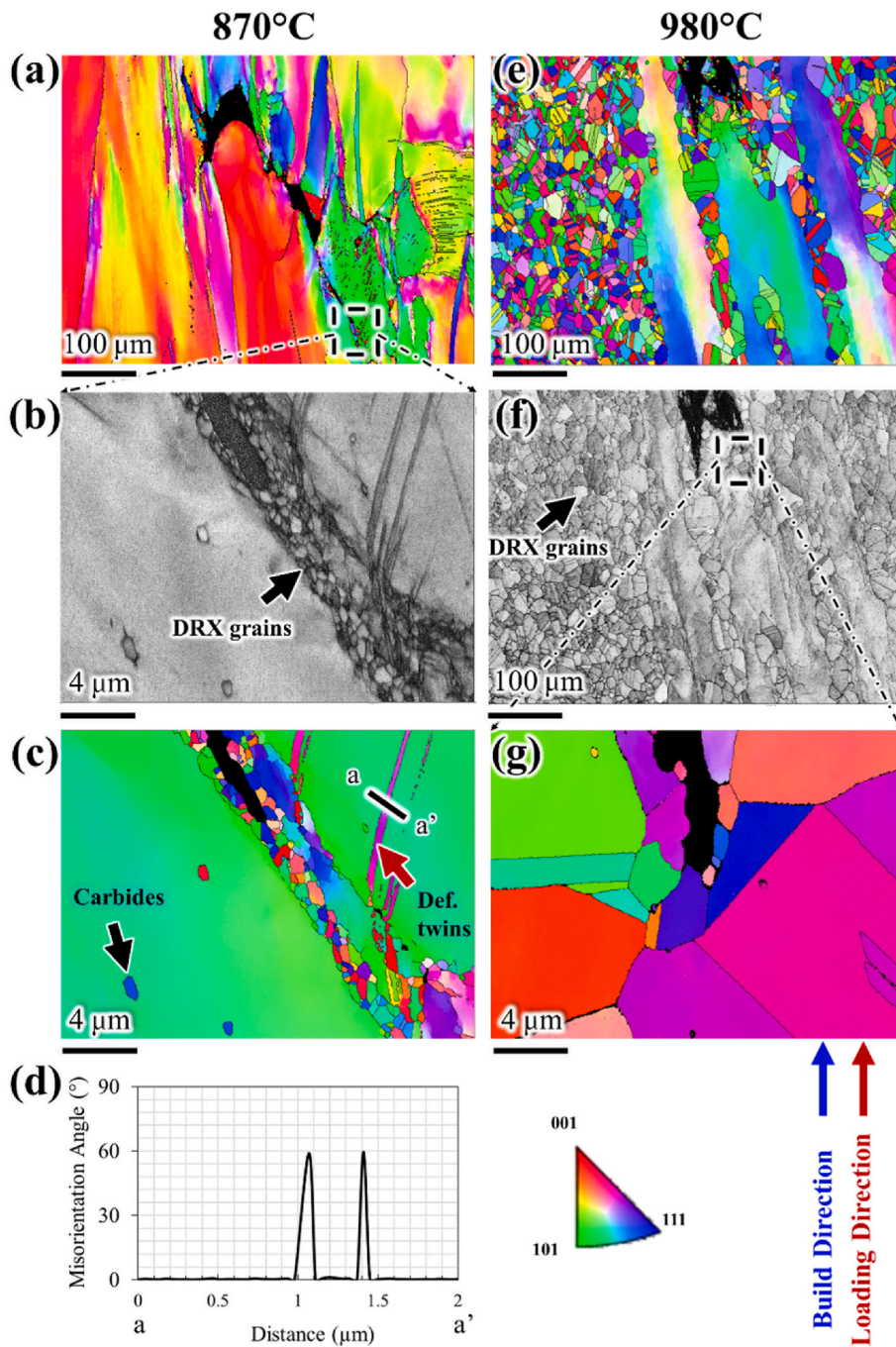
Fig. 12. IPF map taken near a crack on the longitudinal cross section of tensile specimens tested at: (a)–(c) 870 °C and (e)–(g) 980 °C. The misorientation angle profile between points a and a′ in (c) is plotted in (d).

Fig. 9(m)–(o)). Furthermore, the DRX is much more proliferate with the recrystallized and grown grains (~14 μm in diameter) occupying a significant volume fraction of the material (see Figs. 12(e) and Figure 7 (i)). In fact, the fraction of DRX grains at 980 °C was 85% (Fig. 7(i)) compared to <1% at 870 °C (Fig. 7(g)). Accordingly, GB sliding became the dominating deformation mechanism at this temperature, as indicated by the very low intragranular misorientations in KAM map on the longitudinal cross section of a specimen tested at this temperature (see Fig. 7(j)). The GB sliding at 980 °C, facilitated by the high fraction of small DRX grains, significantly increased the EL, resulting in the completely conical fracture surfaces of these specimens (see Fig. 9(m)–(o)).

5. Conclusions

This article reported the tensile properties and analyzed the tensile deformation mechanisms of the fully HT (AMS 5664), LP-DED Alloy 718 over a wide temperature range, i.e., from cryogenic (−195 °C) to elevated (980 °C) temperatures. The general temperature dependence mechanical behavior of the alloy was compared to the counterparts manufactured through other manufacturing routes, including wrought, cast, E-PBF, and L-PBF. Although the study was performed on the alloy deposited using LP-DED, the knowledge learned is nevertheless expected to be valid for Alloy 718 in general. The following conclusions were made based on the experimental observations:

1) Overall, the mechanical properties of LP-DED Alloy 718 were similar with its counterparts in wrought and L-PBF forms.
2) Deformation twinning served an important role in the deformation of Alloy 718 at cryogenic temperatures and contributed to its exceptionally high strength in this condition.
3) The influence of deformation twinning was attenuated with the increasing temperature (up to 650 °C), where dislocation gliding accounted for major portions of plastic deformation.
4) At test temperatures of 870 and 980 °C, dynamic recrystallization and the associated grain boundary sliding became more influential.
5) The fracture mechanism of LP-DED Alloy 718 at and below 650 °C was consistently governed by the fracture and debonding of intragranular metal carbides, while at higher temperatures sliding between the dynamically recrystallized grains dominated the quasi-static tensile fracture.

CRediT authorship contribution statement

Nabeel Ahmad: Conceptualization, Methodology, Investigation, Validation, Formal analysis, Data curation, Writing – original draft, Visualization. **Reza Ghiaasiaan:** Conceptualization, Methodology, Investigation, Formal analysis, Investigation, Writing – review & editing, Visualization. **Paul R. Gradl:** Conceptualization, Methodology, Investigation, Resources, Formal analysis, Writing – review & editing, Funding acquisition. **Shuai Shao:** Conceptualization, Methodology, Resources, Formal analysis, Investigation, Writing – review & editing. **Nima Shamsaei:** Conceptualization, Methodology, Resources, Investigation, Formal analysis, Writing – review & editing, Supervision, Project administration, Funding acquisition.

Declaration of competing interest

The authors declare that they have no known competing financial interests or personal relationships that could have appeared to influence the work reported in this paper.

Data availability

Data will be made available on request.

Acknowledgements

References

[1] ASTM International (A1014/A1014M − 16e1). A1014/A1014M − 16e1 Standard Specification for Precipitation-Hardening Bolting (UNS N07718) for High Temperature Service n.d. https://doi.org/10.1520/A1014_A1014M-16E01.

[2] 718 alloy. HAYNES®, Haynes International (2020). https://www.haynesintl.com/docs/default-source/pdfs/new-alloy-brochures/high-temperature-alloys/brochures/718-brochure.pdf?sfvrsn=14.

[3] P.D. Nezhadfar, A.S. Johnson, N. Shamsaei, Fatigue behavior and microstructural evolution of additively manufactured Inconel 718 under cyclic loading at elevated temperature, Int J Fatigue 136 (2020), 105598, https://doi.org/10.1016/j.ijfatigue.2020.105598.

[4] A.S. Johnson, S. Shuai, N. Shamsaei, et al., microstructure, fatigue behavior, and failure mechanisms of direct laser-deposited inconel 718, JOM 69 (2017) 597–603. https://doi.org/10.1007/s11837-016-2225-2.

[5] B. Blakey-Milner, P. Gradl, G. Snedden, M. Brooks, J. Pitot, E. Lopez, et al., Metal additive manufacturing in aerospace: a review, Mater Des 209 (2021), 110008, https://doi.org/10.1016/j.matdes.2021.110008.

[6] S. Roy, R. Kumar, Panda A. Anurag, R.K. Das, A brief review on machining of inconel 718, Mater Today Proc 5 (2018) 18664–18673, https://doi.org/10.1016/j.matpr.2018.06.212.

[7] A. Yadollahi, N. Shamsaei, Additive manufacturing of fatigue resistant materials: challenges and opportunities, Int J Fatigue 98 (2017) 14–31, https://doi.org/10.1016/j.ijfatigue.2017.01.001.

[8] N. Ahmad, E.U. Enemuoh, Energy modeling and eco impact evaluation in direct metal laser sintering hybrid milling, Heliyon 6 (2020), e03168, https://doi.org/10.1016/j.heliyon.2020.e03168.

[9] S. Lee, S. Shao, D.N. Wells, M. Zetek, M. Kepka, N. Shamsaei, Fatigue behavior and modeling of additively manufactured IN718: the effect of surface treatments and surface measurement techniques, J Mater Process Technol 302 (2022), 117475, https://doi.org/10.1016/j.jmatprotec.2021.117475.

[10] D. Deng, Additively Manufactured Inconel 718 : Microstructures and Mechanical Properties, Linköping University, 2018. http://liu.diva-portal.org/smash/record.jsf?pid=diva2%3A1177201&dswid=6643.

[11] T. DebRoy, H.L. Wei, J.S. Zuback, T. Mukherjee, J.W. Elmer, Milewski JO, et al., Additive manufacturing of metallic components – process, structure and properties, Prog Mater Sci 92 (2018) 112–224, https://doi.org/10.1016/j.pmatsci.2017.10.001.

[12] A. Strondl, M. Palm, J. Gnauk, G. Frommeyer, Microstructure and mechanical properties of nickel based superalloy IN718 produced by rapid prototyping with electron beam melting (EBM), Mater Sci Technol 27 (2011) 876–883, https://doi.org/10.1179/026708309X12468927349451.

[13] S.H. Sun, Y. Koizumi, T. Saito, K. Yamanaka, Y.P. Li, Y. Cui, et al., Electron beam additive manufacturing of Inconel 718 alloy rods: impact of build direction on microstructure and high-temperature tensile properties, Addit Manuf 23 (2018) 457–470, https://doi.org/10.1016/j.addma.2018.08.017.

[14] T. Bhujangrao, F. Veiga, A. Suárez, E. Iriondo, F.G. Mata, High-temperature mechanical properties of IN718 alloy: comparison of additive manufactured and wrought samples, Crystals 10 (2020) 1–13, https://doi.org/10.3390/cryst10080689.

[15] T. Trosch, J. Strößner, R. Völkl, U. Glatzel, Microstructure and mechanical properties of selective laser melted Inconel 718 compared to forging and casting, Mater Lett 164 (2016) 428–431, https://doi.org/10.1016/j.matlet.2015.10.136.

[16] Y.L. Kuo, S. Horikawa, K. Kakehi, The effect of interdendritic δ phase on the mechanical properties of Alloy 718 built up by additive manufacturing, Mater Des 116 (2017) 411–418, https://doi.org/10.1016/j.matdes.2016.12.026.

[17] L. Zhu, Z.F. Xu, P. Liu, Y.F. Gu, Effect of processing parameters on microstructure of laser solid forming Inconel 718 superalloy, Opt Laser Technol 98 (2018) 409–415, https://doi.org/10.1016/j.optlastec.2017.08.027.

[18] P.D. Nezhadfar, N. Shamsaei, N. Phan, Enhancing ductility and fatigue strength of additively manufactured metallic materials by preheating the build platform, Fatigue Fract Eng Mater Struct 44 (2021) 257–270, https://doi.org/10.1111/ffe.13372.

[19] J. Schneider, Comparison of microstructural response to heat treatment of Inconel 718 prepared by three different metal additive manufacturing processes, JOM 72 (2020) 1085–1091, https://doi.org/10.1007/s11837-020-04021-x.

[20] AMS5663N, Nickel alloy, corrosion and heat-resistant, bars, forgings, and rings 52.5Ni - 19Cr - 3.0Mo - 5.1Cb (Nb) - 0.90Ti - 0.50Al - 18Fe consumable electrode or vacuum induction melted 1775 °F (968 °C) solution and precipitation heat treated, SAE Int J Aerosp (2016). https://www.sae.org/standards/content/ams5663n/.

[21] AMS5664. ALLOY BARS, FORGINGS, AND RINGS, CORROSION AND HEAT RESISTANT Nickel Base - 19Cr - 3.1Mo - 5.1(Cb + Ta) - 0.90Ti - 0.50Al Consumable Electrode Melted, Solution Treated at 1950 F (1065.6 C) AMS5664 n.d. https://www.sae.org/standards/content/ams5664/(accessed November 29, 2021).

[22] P.L. Blackwell, The mechanical and microstructural characteristics of laser-deposited IN718, J Mater Process Technol 170 (2005) 240–246, https://doi.org/10.1016/j.jmatprotec.2005.05.005.

[23] D. Deng, J. Moverare, R.L. Peng, H. Söderberg, Microstructure and anisotropic mechanical properties of EBM manufactured Inconel 718 and effects of post heat treatments, Mater Sci Eng A 693 (2017) 151–163, https://doi.org/10.1016/j.msea.2017.03.085.

[24] Y. Ono, T. Yuri, H. Sumiyoshi, E. Takeuchi, S. Matsuoka, T. Ogata, High-cycle fatigue properties at cryogenic temperatures in INCONEL 718, AIP Conf Proc 824 I (2006) 184–191, https://doi.org/10.1063/1.2192350.

[25] E. Hosseini, V.A. Popovich, A review of mechanical properties of additively manufactured Inconel 718, Addit Manuf 30 (2019), 100877, https://doi.org/10.1016/j.addma.2019.100877.

[26] AP&C a GE Additive compay. AP&C a GE Additive Compay (n.d.).

[27] ASTM International, B637: specification for precipitation-hardening and cold worked nickel alloy bars, forgings, and forging stock for moderate or high temperature service, ASTM Int 7 (2018), https://doi.org/10.1520/B0637-18.2.

[28] AMS 5596. Nickel alloy, corrosion and heat resistant, bars, forgings, and rings 52.5Ni 19Cr 3.0Mo 5.1Cb 0.90Ti 0.50Al 18Fe, consumable electrode or vacuum induction melted 1775°F (968°C) solution heat treated, Precipitation Hardenable - SAE International 2507 (2020) 1–9. https://www.sae.org/standards/content/ams5596m.

[29] K. Gruber, R. Dziedzic, B. Kuźnicka, B. Madejski, M. Malicki, Impact of high temperature stress relieving on final properties of Inconel 718 processed by laser powder bed fusion, Mater Sci Eng A (2021) 813, https://doi.org/10.1016/j.msea.2021.141111.

[30] F3056-14e1, Standard Specification for Additive Manufacturing Nickel Alloy (UNS N07718) with Powder Bed Fusion, 2014, https://doi.org/10.1520/F3055-14A. Copyright.

[31] E.M. Fayed, D. Shahriari, M. Saadati, V. Brailovski, M. Jahazi, M. Medraj, Influence of homogenization and solution treatments time on the microstructure and

hardness of Inconel 718 fabricated by laser powder bed fusion process, Materials (Basel) 13 (2020) 1–17, https://doi.org/10.3390/ma13112574.

[32] Committee, E08 AE, Standard Test Methods for Tension Testing of Metallic Materials, ASTM International, 2020. https://www.astm.org/e0008_e0008m-16.html.

[33] ASTM E21, ASTM standard E21–17, Stand Test Methods Tens Test Met Mater (2013) 1–27, i, https://www.astm.org/e0021-20.html.

[34] Interanational AE– 11, Reapproved, Standard guide for preparation of metallographic specimens standard guide for preparation of metallographic specimens, ASTM Int (2017) 1–12. https://www.astm.org/e0003-11r17.html.

[35] S. Zaefferer, N.-N. Elhami, Theory and application of electron channelling contrast imaging under controlled diffraction conditions, Acta Mater 75 (2014) 20–50, https://doi.org/10.1016/j.actamat.2014.04.018.

[36] X. Zhao, J. Chen, X. Lin, W. Huang, Study on microstructure and mechanical properties of laser rapid forming Inconel 718, Mater Sci Eng A 478 (2008) 119–124, https://doi.org/10.1016/j.msea.2007.05.079.

[37] A.N. Jinoop, C.P. Paul, S.K. Mishra, K.S. Bindra, Laser Additive Manufacturing using directed energy deposition of Inconel-718 wall structures with tailored characteristics, Vacuum (2019), https://doi.org/10.1016/j.vacuum.2019.05.027.

[38] H. Qi, M. Azer, A. Ritter, Studies of standard heat treatment effects on microstructure and mechanical properties of laser net shape manufactured INCONEL 718, Metall Mater Trans A Phys Metall Mater Sci 40 (2009) 2410–2422, https://doi.org/10.1007/s11661-009-9949-3.

[39] A. Mostafa, I.P. Rubio, V. Brailovski, M. Jahazi, M. Medraj, Structure, texture and phases in 3D printed IN718 alloy subjected to homogenization and HIP treatments, Metals (Basel) 7 (2017) 1–23, https://doi.org/10.3390/met7060196.

[40] J.R. Zhao, F.Y. Hung, T.S. Lui, Microstructure and tensile fracture behavior of three-stage heat treated inconel 718 alloy produced via laser powder bed fusion process, J Mater Res Technol 9 (2019) 3357–3367, https://doi.org/10.1016/j.jmrt.2020.01.030.

[41] Y. Li, J. Dlouhý, J. Vavřík, J. Džugan, P. Konopík, T. Krajňák, et al., Investigation of short-term creep properties of a coarse-grained Inconel 718 fabricated by directed energy deposition compared to traditional Inconel 718, Mater Sci Eng A (2022) 844, https://doi.org/10.1016/j.msea.2022.143143.

[42] X. Zhao, J. Chen, X. Lin, W. Huang, Study on microstructure and mechanical properties of laser rapid forming Inconel 718, Mater Sci Eng A 478 (2008) 119–124, https://doi.org/10.1016/j.msea.2007.05.079.

[43] S. Sui, H. Tan, J. Chen, C. Zhong, Z. Li, W. Fan, et al., The influence of Laves phases on the room temperature tensile properties of Inconel 718 fabricated by powder feeding laser additive manufacturing, Acta Mater 164 (2019) 413–427, https://doi.org/10.1016/j.actamat.2018.10.032.

[44] M. Komarasamy, S. Shukla, S. Williams, K. Kandasamy, S. Kelly, R.S. Mishra, Microstructure, fatigue, and impact toughness properties of additively manufactured nickel alloy 718, Addit Manuf 28 (2019) 661–675, https://doi.org/10.1016/j.addma.2019.06.009.

[45] B. Diepold, N. Vorlaufer, S. Neumeier, T. Gartner, M. Göken, Optimization of the heat treatment of additively manufactured Ni-base superalloy IN718, Int J Miner Metall Mater 27 (2020) 640–648, https://doi.org/10.1007/s12613-020-1991-6.

[46] D. Keiser, H.L. Brown, A Review of the Physical Metallurgy of Alloy 718, Idaho National Engineering Laboratory, 1976. https://www.osti.gov/biblio/4016087.

[47] T. Sakai, A. Belyakov, R. Kaibyshev, H. Miura, J.J. Jonas, Dynamic and post-dynamic recrystallization under hot, cold and severe plastic deformation conditions, Prog Mater Sci 60 (2014) 130–207, https://doi.org/10.1016/j.pmatsci.2013.09.002.

[48] C. Zhong, A. Gasser, J. Kittel, J. Fu, Y. Ding, R. Poprawe, Microstructures and tensile properties of Inconel 718 formed by high deposition-rate laser metal deposition, J Laser Appl 28 (2016), 022010, https://doi.org/10.2351/1.4943290.

[49] E. Chlebus, K. Gruber, B. Kuźnicka, J. Kurzac, T. Kurzynowski, Effect of heat treatment on the microstructure and mechanical properties of Inconel 718 processed by selective laser melting, Mater Sci Eng A 639 (2015) 647–655, https://doi.org/10.1016/j.msea.2015.05.035.

[50] L. Zhou, A. Mehta, B. McWilliams, K. Cho, Y. Sohn, Microstructure, precipitates and mechanical properties of powder bed fused inconel 718 before and after heat treatment, J Mater Sci Technol 35 (2019) 1153–1164, https://doi.org/10.1016/j.jmst.2018.12.006.

[51] Z. Li, J. Chen, S. Sui, C. Zhong, X. Lu, X. Lin, The microstructure evolution and tensile properties of Inconel 718 fabricated by high-deposition-rate laser directed energy deposition, Addit Manuf 31 (2020), 100941, https://doi.org/10.1016/j.addma.2019.100941.

[52] M.A. Meyers, K.K. Chawla, Mechanical Behavior of Materials, second ed., Cambridge University Press, Cambridge, 2009. https://ceimusb.files.wordpress.com/2015/04/mechanicalbehaviormeyers.pdf.

[53] A. Rollett, F. Humphreys, G.S. Rohrer, M. Hatherly, Recrystallization and Related Annealing Phenomena, second ed., Recryst Relat Annealing Phenom Second, 2004 https://doi.org/10.1016/B978-0-08-044164-1.X5000-2, 1–628.

[54] M.A. Meyers, L.E. Marr, U.S. Lindholm, Shock waves and high-strain-rate phenomena in metals, J Appl Mech 49 (1982), https://doi.org/10.1115/1.3162565, 683–683.

[55] L. Huang, F. Qi, P. Hua, L. Yu, F. Liu, W. Sun, et al., Discontinuous dynamic recrystallization of Inconel 718 superalloy during the superplastic deformation, Metall Mater Trans A Phys Metall Mater Sci 46 (2015) 4276–4285, https://doi.org/10.1007/s11661-015-3031-0.

[56] D. Jianxin, X. Xishan, Z. Shouhua, Coarsening behavior of γ'' precipitates in modified inconel 718 superalloy, Scr Metall Mater 33 (1995) 1933–1940, https://doi.org/10.1016/0956-716X(95)00446-3.